Spherical scattering of superpositions of localized waves

Desmond Power and Rod Donnelly
Faculty of Engineering and Applied Science, Memorial University of Newfoundland, St. John's, Newfoundland, Canada A1B 3X5

Robert MacIsaac*
Canadian Centre for Marine Communications, 155 Ridge Road, St. John's, Newfoundland, Canada A1C 5R3
(Received 25 January 1993)

We investigate, for purposes of remote sensing, the spherically backscattered spectra of acoustic realizations of localized wave solutions to the homogeneous wave equation. The solutions represent broadband focused interference patterns whose focusing properties have been demonstrated to be superior to those of equivalent monochromatic (i.e., cw) solutions, in the context of multi-time-derivative transmit-receive systems. The interference patterns are acoustically launched with a synthetic hydrophone array. The backscattered spectra of several different sized steel and aluminum spheres have been obtained. Analysis indicates that the sphere radius can be readily extracted from these spectra.

PACS number(s): 03.40.Kf, 43.20.+g, 43.30.+m, 03.80.+r

I. INTRODUCTION

Over the past number of years, there have been various works detailing localized wave (LW) solutions of the homogeneous wave equation (HWE), the Klein-Gordon equation, and the damped wave equation [1–9]. Authors have shown how to launch these broadband wave forms [3,6,7,10-13] and have described how effectively they retain their localization properties [6,7]. The basic LW HWE solution was discovered by Ziolkowski [2], using the work of Brittingham [1], and is called a *focus wave mode* (FWM). Although the FWM has infinite energy, it possesses an arbitrary parameter, and one can form finite energy weighted superpositions (over this parameter) of FWM's. In particular, Ziolkowski considered the so-called *modified power spectrum* (MPS) pulse, given by

$$\psi_{\mathrm{MPS}}(\mathbf{r},t)=\frac{1}{z_0+i(z-ct)}\frac{1}{(s/B+1)}e^{-bs/B}, \qquad (1)$$

where $s=\rho^2/[z_0+i(z-ct)]-i(z+ct)$, $\rho=\sqrt{x^2+y^2}$, and z_0, b, and B are free parameters. The MPS pulse is shown, for particular values of z_0, b, and B, in Fig. 1.

The superior focusing properties of the MPS pulse, as compared with equivalent continuous wave (cw) pulses, and in the context of multi-time-derivative transmit-receive systems, has been demonstrated [6]. In this paper, we predict and then acoustically measure the spherically scattered spectra of a MPS pulse in an attempt to indicate the potential usefulness of LW pulses for remote sensing applications.

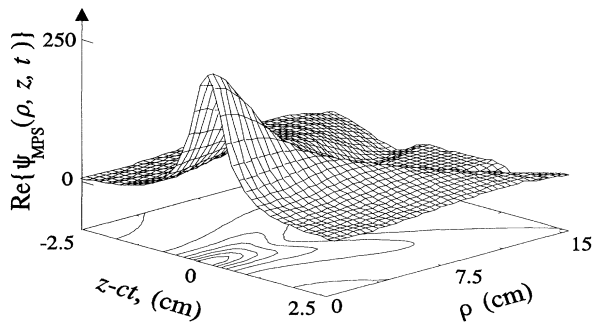

FIG. 1. Surface plot of the HWE solution pulse $\mathrm{Re}\{\psi_{\mathrm{MPS}}(\rho,z,t)\}$ for the values $t=0$ s, $z_0=4.0\times10^{-3}$ m, $b=750$ m^{-1}, and $B=300$.

In Sec. II we show how the spherical backscattered spectrum of a FWM may be obtained by using a Fourier-transform technique introduced by Donnelly and Ziolkowski [8,9]. We first derive an expression for the spherical backscatter due to an arbitrary incident plane wave. We then obtain the spherical backscatter spectrum of the FWM by using a weighted superposition of the plane-wave spherical backscatter over the plane-wave (Fourier) components of the FWM. The MPS spherical backscatter can then be obtained simply by using the same technique (i.e., weighted superposition) used to obtain the MPS pulse from the FWM.

In Sec. III we show how the MPS spherical backscatter spectrum can vary with the size and material composition of the sphere. We also discuss how the size of the sphere may be extracted from the MPS backscatter spectrum. In Sec. IV we show how LW solutions of the HWE may be launched using Huygens's reconstruction. In Sec. V we explain how actual MPS acoustic backscatter experiments were performed using ultrasonic hydrophones placed in a large water tank. In Sec. VI we discuss the results of our acoustic experiments and our attempt at extracting the size of the spheres.

II. PREDICTED BACKSCATTERED SPECTRUM

In what follows we shall be suppressing an $e^{-i\omega t}$ time dependence on field quantities and, for reasons we shall see, we shall assume that $\omega<0$. As such, if $\mathbf{k}$ denotes a vector whose spherical polar components are (k,ϑ,φ), then the plane wave

$$e^{i\mathbf{k}\cdot\mathbf{r}-i\omega t} \qquad (2)$$

is not traveling in the direction of $\mathbf{k}$ as t increases. Writing

$$e^{i\mathbf{k}\cdot\mathbf{r}-i\omega t}=[e^{-i\mathbf{k}\cdot\mathbf{r}-i|\omega|t}]^* , \tag{3}$$

we see that the plane wave $e^{-i\mathbf{k}\cdot\mathbf{r}-i|\omega|t}$ is traveling in the direction of $-\mathbf{k}$ as t increases, where the spherical polar components of $-\mathbf{k}$ are $(k,\pi-\vartheta,\varphi+\pi)$.

Morse and Ingard [14] give an expression for the scattered field at a point (r_0,θ_0,ϕ_0) due to a plane wave of unit amplitude and wave number k, incident on a nonrigid sphere of radius a centered on the origin, in the direction of the positive z axis; the medium outside the sphere is assumed to be homogeneous, isotropic, and have a velocity of wave propagation c. Symmetry considerations imply that this expression will also give the scattered field at a point whose Cartesian coordinates are $(0,0,-r)$, due to a plane wave traveling towards the center of the sphere *from* a direction whose spherical polar angles are θ_0 and ϕ_0. According to (3), we may modify this result to obtain the field at $(0,0,-r)$ due to the plane wave $e^{i\mathbf{k}\cdot\mathbf{r}-i\omega t}$, where $\omega<0$. The result is (suppressing the $e^{-i\omega t}$ time dependence)

$$-\left[\sum_{n=0}^{\infty}(i)^n(2n+1)\frac{j_n'(ka)+i\alpha_n j_n(ka)}{h_n^{(1)\prime}(ka)+i\alpha_n h_n^{(1)}(ka)}\times h_n^{(1)}(kr)P_n(\cos\vartheta)\right]^* . \tag{4}$$

In (4) the term α_n is given by

$$\alpha_n=\frac{i\rho c}{\rho_e c_e}\left[\frac{j_n'(k_e a)}{j_n(k_e a)}\right] , \tag{5}$$

where ρ is the density of the infinite medium surrounding the sphere, ρ_e is the density of the sphere material, c_e is the speed of wave propagation in the sphere (so that $c_e=1/\sqrt{\rho_e\kappa_e}$, where κ_e is the compressibility of the sphere material), $k=|\omega|/c$, $k_e=|\omega|/c_e$, a prime superscript on a function denotes the derivative of the adorned function, j_n is the usual spherical Bessel function, $h_n^{(1)}$ is the spherical Hankel function of the first kind, and P_n is a Legendre polynomial. We may compactly rewrite the expression in (4) as

$$\sum_{n=0}^{\infty}\gamma_n h_n^{(2)}(kr)P_n(\cos\vartheta) \tag{6}$$

where

$$\gamma_n=-(2n+1)(-i)^n\left[\frac{j_n'(ka)+i\alpha_n j_n(ka)}{h_n^{(2)\prime}(ka)+i\alpha_n h_n^{(2)}(ka)}\right] , \tag{7}$$

where $h_n^{(2)}$ is the spherical Hankel function of the second kind.

In principle then, one may obtain the scattered field at the point $(0,0,-r)$ on the negative z axis, due to an arbitrary incident wave form, if it is composed of a weighted superposition of plane waves like (2). We merely take the weighted superposition of (6) over each plane-wave (i.e., Fourier) component of the incident wave form (the weighting being the space-time Fourier transform of the incident wave form).

We shall suppose that the incident wave form $\psi(\mathbf{r},t)$ is a solution of the homogeneous wave equation for infinite space filled with a material such as that surrounding the sphere, that is,

$$\left[\nabla^2-\frac{1}{c^2}\frac{\partial^2}{\partial t^2}\right]\psi(\mathbf{r},t)=0 . \tag{8}$$

Applying a spatial and temporal Fourier transform to (8) tells us that $\Psi(\mathbf{k},\omega)$ must satisfy

$$(k^2-\omega^2/c^2)\Psi(\mathbf{k},\omega)=0 , \tag{9}$$

where $k=|\mathbf{k}|=(k_x^2+k_y^2+k_z^2)^{1/2}\equiv(\kappa^2+k_z^2)^{1/2}$, and where

$$\Psi(\mathbf{k},\omega)=\int_{\mathbb{R}^3}d\mathbf{r}\int_{\mathbb{R}}dt\,\psi(\mathbf{r},t)e^{-i\mathbf{k}\cdot\mathbf{r}+i\omega t} . \tag{10}$$

As such, we realize [8,9] that $\Psi(\mathbf{k},\omega)$ can be any generalized function whose support lies on the surface

$$\kappa^2+k_z^2-(\omega/c)^2=0 , \tag{11}$$

shown in Fig. 2, in semi-infinite $(\kappa,k_z,\omega/c)$ space, such that the product $[\kappa^2+k_z^2-(\omega/c)^2]\Psi(\mathbf{k},\omega)$ is equal to zero in the sense of generalized functions. The function $\Psi(\mathbf{k},\omega)$ may thus contain δ functions whose supports are points, lines, or patches lying on the surface (11). There is an obvious one-to-one correspondence between the supports of the Fourier transforms on HWE solutions and their projections on the $(k_z,\omega/c)$ plane. One may thus completely characterize a HWE solution $\psi(\mathbf{r},t)$ by considering the projection onto the $(k_z,\omega/c)$ plane of the support of $\Psi(\mathbf{k},\omega)$, together with the weighting function to be associated with the support. Donnelly and Ziolkowski [9] discuss this characterization in general and give examples.

A particularly interesting example of a HWE solution is the so-called *focus wave mode* discovered by Ziolkowski [2]:

$$\psi_\beta(\mathbf{r},t)=e^{i\beta(z+ct)}\frac{e^{-\rho^2\beta/[z_0+i(z-ct)]}}{4\pi i[z_0+i(z-ct)]} , \tag{12}$$

where $z_0>0$ is assumed to be fixed and $\beta>0$ is an arbitrary parameter. The FWM in (12) propagates along the

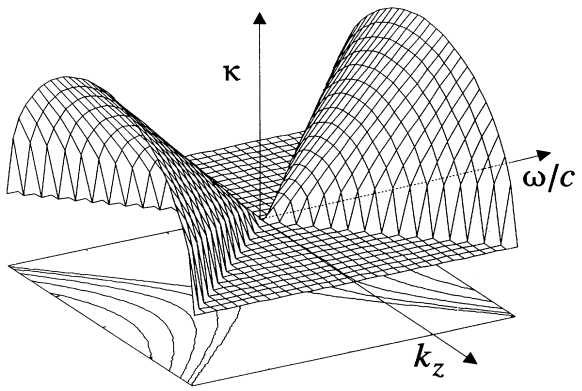

FIG. 2. The surface $\kappa^2+k_z^2-\omega^2/c^2=0$, shown in $(\kappa,k_z,\omega/c)$ space.

z axis with speed c and has a degree of focusing about this axis which depends on β: for small values of β, ψ_β behaves like a plane wave, whereas for large values of β, ψ_β behaves like a particle. The Fourier transform of the FWM solution in (12) is given by

$$\Psi_\beta(\mathbf{k},\omega)=\frac{\pi^2}{i\beta}e^{-\kappa^2 z_0/4\beta}\delta(k_z-(\beta-\kappa^2/4\beta)) \times\delta(\omega+c(\beta+\kappa^2/4\beta)) . \tag{13}$$

From (13) one can readily determine that the support of $\Psi_\beta(\mathbf{k},\omega)$ is a line lying on the surface (11), whose projection onto the $(k_z,\omega/c)$ plane is a straight line, of slope one, as shown in Fig. 3.

From Figure 3 we see that the temporal Fourier transform of the FWM, $\mathcal{F}_t\{\psi_\beta\}(\mathbf{r},\omega)$, will be an analytic signal in that it contains only negative frequency components. The signal that we attempt to launch is $\mathrm{Re}\{\psi_\beta\}(\mathbf{r},t)$, which has the two-sided temporal Fourier transform $\frac{1}{2}[\mathcal{F}_t\{\psi_\beta\}(\mathbf{r},\omega)+(\mathcal{F}_t\{\psi_\beta\}(\mathbf{r},\omega))^*]$.

As already discussed then, the scattered field at the point whose Cartesian coordinates are $(0,0,-r)$, due to an incident FWM of the form (12), will be given by a weighted superposition of the expression (6), for a single plane wave, over the plane-wave (Fourier) decomposition (13) of the FWM, that is, the scattered field is given by

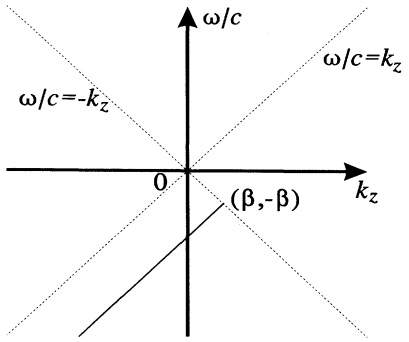

FIG. 3. Projection of the support line of the HWE solution Fourier transform domain function $\Psi_{\mathrm{MPS}}(k,\omega)$, onto the $(k_z,\omega/c)$ plane. The projection is shown as the solid line segment.

$$\Lambda_\beta(r,\omega)=\frac{\pi^2}{i\beta}\frac{1}{(2\pi)^3}\int_{\mathbb{R}^3}d\mathbf{k}\,e^{-\kappa^2 z_0/4\beta}\delta(k_z-(\beta-\kappa^2/4\beta))\delta(\omega+c(\beta+\kappa^2/4\beta))\sum_{n=0}^{\infty}\gamma_n h_n^{(2)}(kr)P_n(\cos\vartheta) , \tag{14}$$

where $\int_{\mathbb{R}^3}d\mathbf{k}$ denotes the integral over the three-dimensional spatial Fourier transform domain.

The following identity, valid in the sense of generalized functions, is readily verified:

$$\delta(\omega+c\beta+c\kappa^2/4\beta)\equiv\frac{\sqrt{\beta}}{c\sqrt{|\beta+\omega/c|}}u(-\omega/c-\beta)\delta[\kappa-\sqrt{4\beta|\beta+\omega/c|}] , \tag{15}$$

where u, the unit step function, is needed to ensure $\omega+c\beta<0$. We may break the volume integral $\int_{\mathbb{R}^3}$ in (14) into separate integrations over cylindrical polar coordinate variables as $\int_0^{2\pi}d\varphi\int_{\mathbb{R}}dk_z\int_0^{\infty}d\kappa\,\kappa$. With the aid of the identity (15) we may perform the κ and φ integrations to get

$$\Lambda_\beta(r,\omega)=\frac{u(-\beta-\omega/c)}{2ic}e^{z_0(\beta+\omega/c)}\int_{\mathbb{R}}dk_z\delta[k_z-(2\beta+\omega/c)]\sum_{n=0}^{\infty}\gamma_n h_n^{(2)}(kr)P_n(\cos\vartheta)|_{\kappa=\sqrt{4\beta|\beta+\omega/c|}} . \tag{16}$$

Care must be exercised with the remaining k_z integral. With $\kappa=\sqrt{4\beta|\beta+\omega/c|}$, we see that the remaining δ function will set k_z, so that k becomes

$$k=(\kappa^2+k_z^2)^{1/2}=\{4\beta|\beta+\omega/c|+(2\beta+\omega/c)^2\}^{1/2} =|\omega|/c ,$$

where the last equality followed from the step function $u(-\omega/c-\beta)$ in (16). Similarly, we find that $\cos\vartheta=k_z/k\to 2\beta c/|\omega|-1$. Thus (16) becomes

$$\Lambda_\beta(r,\omega)=\frac{u(-\beta-\omega/c)}{2ic}e^{z_0(\beta+\omega/c)} \times\sum_{n=0}^{\infty}\gamma_n|_{k=|\omega|/c}h_n^{(2)}(|\omega|r/c)P_n\left[\frac{2\beta c}{|\omega|}-1\right] . \tag{17}$$

We now make the observation that, as β is an arbitrary positive parameter in (12), any weighted superposition

$$\int_0^{\infty}d\beta F(\beta)\psi_\beta(\mathbf{r},t) \tag{18}$$

will also be a HWE solution. We can choose the weighting $F(\beta)$ so that the superposition (18) has finite energy and desirable propagation characteristics [3]. In particular, we can choose the weighting

$$F(\beta)=\begin{cases}4\pi iBe^{-(B\beta-b)} & \text{if } \beta>b/B\\ 0 & \text{if } 0\le\beta<b/B\end{cases} \tag{19}$$

to get the so-called *modified power spectrum* superposition [3], given in (1).

With the wave form (1) incident on the sphere, the received signal at the point $(0,0-r)$ on the negative z axis is given by

$$\Lambda_{\mathrm{MPS}}(r,\omega)=\int_0^\infty d\beta F(\beta)\Lambda_\beta(r,\omega)$$
$$=\frac{2\pi Bu\left[-\frac{\omega}{c}-\frac{b}{B}\right]}{c}\sum_{n=0}^{\infty}\gamma_n|_{k=|\omega|/c}h_n^{(2)}(|\omega|r/c)\int_{b/B}^{|\omega|/c}d\beta\, e^{-\beta(B-z_0)}P_n\left[\frac{2\beta c}{|\omega|}-1\right]. \quad (20)$$

If we make the change of variable $\zeta=2\beta c/|\omega|-1$ in (20), we can integrate the result by parts n times ($P_n^{(n+1)}\equiv 0$) to get

$$\Lambda_{\mathrm{MPS}}(r,\omega)=\frac{\pi B|\omega|}{c^2}\sum_{n=0}^{\infty}\gamma_n|_{k=|\omega|/c}h_n^{(2)}(|\omega|r/c)u(-\omega/c-b/B)$$
$$\times\left\{e^{-z_0(|\omega|/c-b/B)}\left[\frac{P_n(\zeta_0)}{\sigma}+\frac{P_n'(\zeta_0)}{\sigma^2}+\cdots+\frac{P_n^{(n)}(\zeta_0)}{\sigma^{n+1}}\right]\right.$$
$$\left.-e^{-|\omega|\beta/c+b}\left[\frac{P_n(1)}{\sigma}+\frac{P_n'(1)}{\sigma^2}+\cdots+\frac{P_n^{(n)}(1)}{\sigma^{n+1}}\right]\right\} \quad (21)$$

where

$$\sigma=\frac{|\omega|}{2c}(B-z_0),\quad \zeta_0=\frac{2bc}{B|\omega|}-1\ . \quad (22)$$

III. ANALYSIS OF BACKSCATTERED SPECTRUM

Closer examination of (21) reveals that the predicted backscattered spectrum is a complicated function of the distance from the sphere r, the sphere radius a, and the sphere's material parameters ρ_e and $c_e=1/\sqrt{\rho_e\kappa_e}$. For remote sensing purposes we should like to extract the material parameters from the sphere's backscattered spectrum, most notably the sphere radius a. In Fig. 4 we illustrate the backscattered spectrum for varying sphere radius. In this example, we use material parameters $c_e=3.0\times10^3$ m/s and $\rho_e=7.8\times10^3$ kg/m^3, similar to those of mild steel. For this and all subsequent examples and experiments we use MPS pulse parameters $z_0=4.0\times10^{-3}$ m, $B=300$, and $b=750$ m^{-1} such that the waist of the pulse is 4.0 cm.

The spectrum appears as a series of frequency peaks and dips beyond approximately 30 kHz. The spectral spacing of these dips changes with sphere radius; as the size of the sphere increases, the spacing between adjacent dips decreases. Hence we may be able to extract the sphere radius by examining the frequency of these spectral peaks and dips.

However, the two variables c_e and ρ_e also appear in (21); hence we should examine the effect these have on the spectral dip frequencies as well. In Fig. 5 we show the backscattered spectrum for varying ρ_e. In this example we have used the parameters $a=0.3$ cm and $c_e=3.0\times10^3$ m/s with three values of ρ_e: (3.9, 7.8, 11.7) $\times10^3$ kg/m^3. As this figure shows, a large change in ρ_e does not greatly affect the spacing of the spectral dips.

In Fig. 6 we now show the backscattered spectrum for varying c_e. In this example we again use the sphere parameters $a=0.3$ cm and $\rho_e=7.8\times10^3$ kg/m^3 with three values of c_e: $(1.5,3.0,4.5)\times10^3$ m/s. However, this figure shows that as c_e increases, the spacing of the spectral dips decreases.

It is notable that many metals and hard materials have similar c_e values [15] (Table I). Hence, it should be possi-

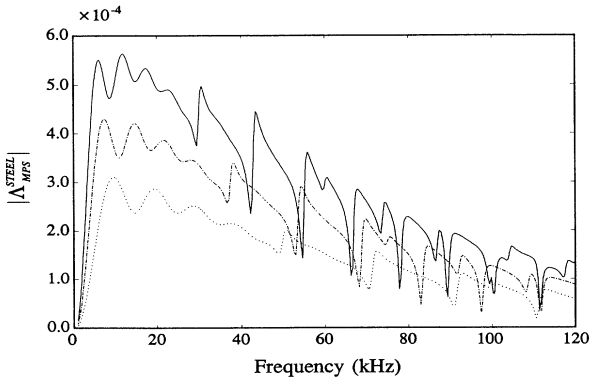

FIG. 4. Magnitude plot of the predicted backscattered spectra, $\Lambda_{\mathrm{MPS}}(r,\omega)$ for $r=150$ mm, $c_e=3000$ m/s, and $\rho_e=7.8\times10^3$ kg/m^3. Radius legend: $a=50$ mm (solid), $a=40$ mm (dashed), and $a=30$ mm (dotted).

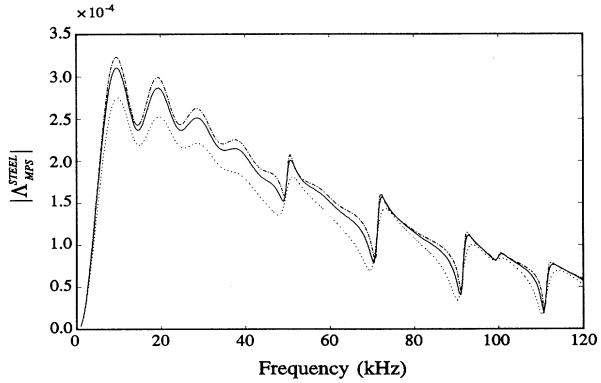

FIG. 5. Magnitude plot of the predicted backscattered spectra, $\Lambda_{\mathrm{MPS}}(r,\omega)$ for $r=150$ mm, $c_e=3000$ m/s, and $a=30$ mm. Density legend: $\rho_e=3.9\times10^3$ kg/m^3 (dotted), $\rho_e=7.8\times10^{-3}$ kg/m^3 (solid), and $\rho_e=11.7\times10^3$ kg/m^3 (dashed).

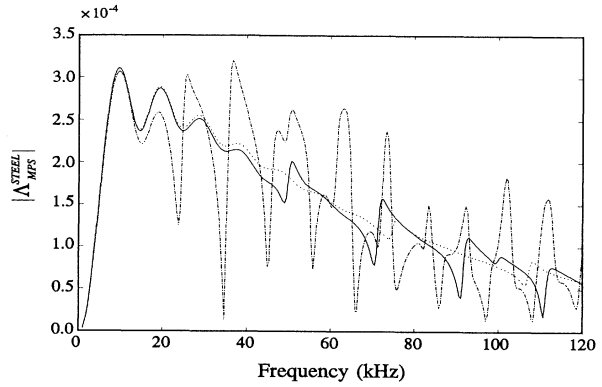

FIG. 6. Magnitude plot of the predicted backscattered spectra, $\Lambda_{\mathrm{MPS}}(r,\omega)$ for $r=150$ mm, $a=30$ mm, and $\rho_e=7.8\times10^3$ kg/m^3. Velocity legend: $c_e=1500$ m/s (dotted), $c_e=3000$ m/s (solid), and $c_e=4500$ m/s (dashed).

ble to extract the sphere size from the backscattered spectrum with a small margin of error due to a variable c_e.

IV. LAUNCHING SUPERPOSITIONS OF LOCALIZED WAVES

In previous LW experiments, Huygens's reconstruction formula [16] has been used to determine the array driving functions [10,11]. In Ziolkowski's experiments, he used Huygens's reconstruction formula [16] to launch superpositions of the MPS pulse. This formula allows one to generate any solution of the homogeneous wave equation at a fixed point in a bounded region of space, provided one knows the value of the solution, its temporal derivative, and its normal derivative at each point on the bounding surface S' of the region. If the HWE solution is $\psi(\mathbf{r},t)$, then if the field point $\mathbf{r}$ lies inside the region bounded by S' we have

$$\psi(\mathbf{r},t)=-\int_{S'}dS\{g(\mathbf{r},\mathbf{r}')[\partial_{n'}\{\psi\}]-[\partial_{ct}\psi]\partial_{n'}\{g(\mathbf{r},\mathbf{r}')\} -g(\mathbf{r},\mathbf{r}')[\psi]\partial_{n'}\{R\}\}\ . \tag{23}$$

In (23), ∂_{ct} is the temporal differential operator, $\partial_{n'}$ is the normal differential operator, integration is with respect to the primed coordinates, $g(\mathbf{r},\mathbf{r}')=1/4\pi R$, $R\equiv|\mathbf{r}-\mathbf{r}'|$ denotes the distance from the field point to the source (integration) point, and the square brackets around a function indicate that it is to be evaluated at the retarded time $t-R/c$.

TABLE I. Speed of sound $c_e=\sqrt{\kappa_e\rho_e}$ in various hard materials.

Material	c_e (m/s)
Stainless steel	3100
Aluminum (rolled)	3040
Titanium	3125
Nickel	3000
Magnesium	3050
Cast iron	2809
Pyrex glass	3280

We should like to launch the MPS pulse in (1) into the region $z>0$; the surface S' is therefore taken to be the plane $z'=0$. This leads to the formulation

$$\psi(\mathbf{r},t)=-\int_{S'}dS'\left\{[\partial_{z'}\psi]-[\partial_t\psi]\frac{z}{cR}-[\psi]\frac{z}{R^2}\right\}\frac{1}{4\pi R}\ . \tag{24}$$

We may use (24) to reconstruct MPS pulses using point source transducers whose impulse response is modeled by

$$h(\mathbf{r},\mathbf{r}',t)=\delta(t-R/c)/4\pi R\ . \tag{25}$$

We are constrained to a finite number of transducers; as the MPS pulse $\psi(\mathbf{r},t)$ in (1) is focused near the propagation axis, hopefully we can construct an approximation to it using a finite number of transducers that are symmetrically placed about the z axis in the plane $z'=0$:

$$\psi(\mathbf{r},t)\approx-\sum_{n=1}^{N}\mathcal{A}(n)\{[\partial_{z'}\psi]-[\partial_t\psi]\frac{z}{cR}-[\psi]\frac{z}{R^2}\}\frac{1}{4\pi R} =-\sum_{n=1}^{N}\mathcal{A}(n)\frac{[D_n(x',y',t)]}{4\pi R}\ , \tag{26}$$

where N is the number of transducers and $\mathcal{A}(n)$ is an area weighting for each element, replacing dS' in (24). For a uniform array of equally spaced elements, $\mathcal{A}(n)$ is constant for all n.

If we fix the field point $\mathbf{r}$, then the signals required at each of the transducers D_n are determined through (26). When launching superpositions of LW's so as to construct, for example, the MPS pulse described above, one usually chooses a field point $\mathbf{r}$ that is close to the propagation z axis and far from the plane $z'=0$. This allows for the approximation $z/R\approx1$ for each of the transducers in (26) such that the signal to be fed into each transducer reduces to $D_n(x',y',t)=2\partial_t\{\psi(x',y',z'=0,t)\}$ [6].

V. EXPERIMENTAL METHODOLOGY

In order to obtain spherical backscatter signals for analysis, acoustic experiments were conducted in large ($3\times4\times5$ m^3) tank. Three steel spheres with radii measuring 20, 40, and 60 mm and a single aluminum sphere with a radius of 40 mm were used. The MPS pulses were launched using the double hydrophone system illustrated in Fig. 7.

The experimental setup is controlled using a personal computer (PC) and an general purpose interface bus (GPIB). Digitized signals are generated by the computer and sent to an arbitrary wave-form generator and amplifier. The MPS pulses are reconstructed synthetically, using superposition, by a single hydrophone (B&K 8103). A stepper motor is used to move the hydrophone to the required positions along the synthetic transmit aperture. The spheres are placed directly in front of the transmit aperture in line with the array's z axis. Another hydrophone (Reson TC4104) senses both the transmit and reflected signals from the transmitting hydrophone and the sphere, respectively. Received signals are relayed back to the PC for further reconstruction and signal processing.

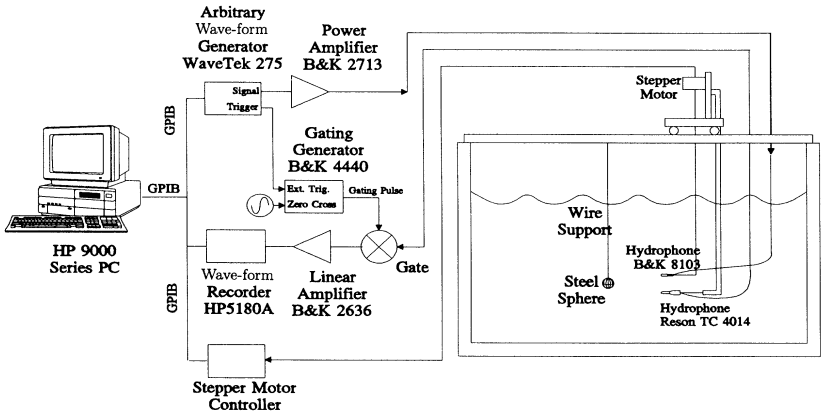

FIG. 7. Backscatter spectra measurement system.

The axisymetric nature of both the MPS pulse and the reflecting sphere allows us to reduce the number of elements in the transmit array by using discrete, equally spaced annular sections. If the receiver hydrophone is placed on the z axis ($\rho=0$) then, assuming a flat band system transfer function, we may reconstruct the backscattered signal using the formula

$$v_{\mathrm{MPS}}(r,t)=-\sum_{n=0}^{N}\varsigma_n(r,t)\mathcal{A}(n)\ . \tag{27}$$

In (27), v_{MPS} is the reconstructed backscattered signal, ς_n are the spherically reflected signals originating from each of the N transmit elements, $\mathcal{A}(n)=2\pi\rho_n\Delta\rho$, ρ_n is the radial location of the nth element, and $\Delta\rho$ is the spacing between adjacent annular elements. Thus a complete aperture can be synthesized by moving the transmit hydrophone to discrete positions along a single radius of the transmit aperture corresponding to each discrete annular region. For these experiments, $N=30$ and $\Delta\rho=4$ mm; hence the aperture has a radius of 116 mm.

In order to obtain a variety of spectra, each sphere was placed at the r distances 150, 250, and 350 mm. At the distance $r=150$ mm, the spheres are located in the *near field* of the transducer array [6]. In this case the near field of the array simply refers to where the approximation $z/R\approx 1$, discussed previously in Sec. IV, is invalid (or where z is less than the size of the aperture).

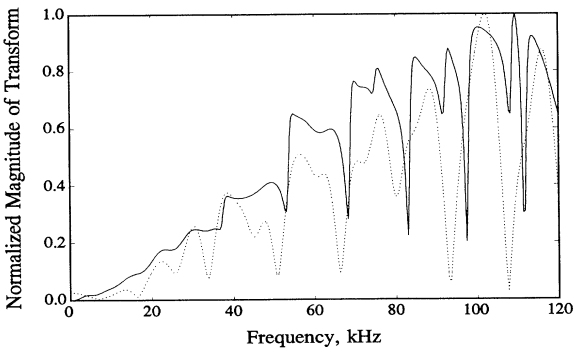

FIG. 8. Magnitude plot of the double hydrophone system transfer function $H(\omega)$ (solid), and a least-squares-fitted second-order polynomial, $A\omega^2$ (dotted).

Both hydrophones are essentially omnidirectional devices and are constructed using rubber coated spherically shaped piezoelectric material. The tip dimensions of each device are 9.5 and 11 mm for the transmitter and receiver, respectively. The amplifiers and hydrophones provide for a bandwidth of approximately 0–135 kHz. Analysis of system TX-RX transfer function was performed by inputting sinc($2wt$) pulses of bandwidth w into the transmitter. A plot of the received signal from a 150-kHz sinc pulse is shown in Fig. 8.

Below 110 kHz, the system transfer function $H(\omega)$ can be approximated by the equation $A\omega^2$, where A is a constant. In other words, the system is approximately a double time differentiator in the 0–110 kHz band. Hence, if the MPS pulse is designed such that the effective upper frequency f_{eff} [6] of each driving function is below 110 kHz, then the backscattered spectrum Λ_{MPS} and the Fourier transform of the reconstructed signal Υ_{MPS} are approximately related by

$$\Upsilon_{\mathrm{MPS}}(r,\omega)\approx A\omega^2\Lambda_{\mathrm{MPS}}(r,\omega) \tag{28}$$

in the range 0–110 kHz. For the MPS parameters chosen, $f_{\mathrm{eff}}=59.7$ kHz.

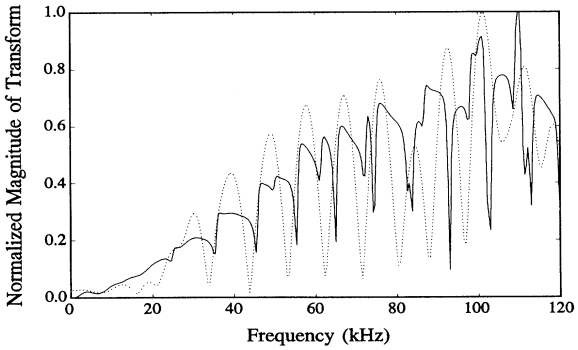

FIG. 9. Comparison of the reconstructed backscattered spectrum $|\Upsilon_{\mathrm{MPS}}^{\mathrm{STEEL}}|$ (dotted), with the predicted backscattered spectrum $|\Lambda_{\mathrm{MPS}}^{\mathrm{STEEL}}|$ (solid) for a 40-mm-radius steel sphere placed at $r=150$ mm from the synthetic array.

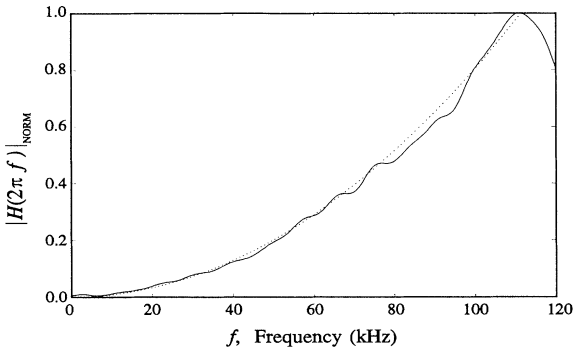

FIG. 10. Comparison of the reconstructed backscattered spectrum $|\Upsilon_{MPS}^{STEEL}|$ (dotted), with the predicted backscattered spectrum $\Lambda_{MPS}^{STEEL}|$ (solid), for a 60-mm-radius steel sphere placed at $r=150$ mm from the synthetic array.

VI. EXPERIMENTAL RESULTS

In the figures that follow, the reconstructed backscattered spectrum Υ_{MPS} is compared to the predicted backscattered spectrum Λ_{MPS}. The predicted spectrum has been weighted with the system transfer function $H(\omega)=A\omega^2$ in order to account for two time derivatives. In Figs. 9 and 10, we show predicted versus measured spectra for steel sphere radii 40 and 60 mm, respectively. In both spectra we see that both the predicted and measured spectra contain *dips* at similar spacings. Differences in both spectra may be due to the approximation of the MPS pulse in the reconstruction and to differences in material parameters.

Numerical analysis with predicted spectra has shown that the spectral width of adjacent dips is inversely proportional to the sphere radius. Using this relationship, we have calibrated the numerical parameters based on the three steel sphere spectra obtained at $r=150$ mm; these numerical parameters are used in a sphere radius algorithm that extracts the radii from other backscattered spectra. Table II shows the extraction results for each of the spheres at the indicated distances. The maximum error is 3.5% for the steel spheres and 6.5% for the aluminum sphere. The relatively high percent error for the aluminum sphere is expected because of the difference in c_e between steel and aluminum. However, all errors appear to be within tolerable limits.

VII. CONCLUSIONS

In the context of multi-time-derivative transmit-receive systems (such as that present in the forward propagating section of our experimental setup), the superior focusing properties of the MPS pulse over equivalent cw pulses has been demonstrated [6]. It thus seems natural to try to use the extended near-field characteristics of the MPS pulse, coupled with its broadband nature, to extract information from backscattered signals; the broadband nature of the signal allows for parameter extraction, while it is the enhanced propagation properties of the LW pulses that ensures that a relatively large amount of energy reaches the target. Other broadband signals might not have desirable propagation properties and more focused monochromatic pulses would not have the desirable spectral width.

We have successfully extracted sphere radii from the MPS backscattered spectra of several different sizes of steel and aluminum spheres, using a relatively naive algorithm. In this algorithm, the speed of sound in the sphere is assumed known (and is approximately the same for a wide variety of metals) and the radius is extracted from the spectrum. It may be possible to estimate both the material properties and the radius from the backscattered spectrum. Work on this is ongoing.

TABLE II. Sphere radii extracted from reconstructed backscattered spectra.

Actual size (cm)	Distance from array (cm)	Estimated size (cm)	Percent error
	Steel		
2.0	15	1.9941	0.3
2.0	25	2.0044	0.2
2.0	35	1.9975	0.1
4.0	15	4.0968	2.4
4.0	25	4.0939	2.3
4.0	35	4.1403	3.5
6.0	15	5.8445	2.6
6.0	25	5.7954	3.4
6.0	35	5.8632	2.3
	Aluminum		
4.0	25	4.1773	4.4
4.0	35	4.2610	6.5

ACKNOWLEDGMENTS

The authors wish to thank Dr. Richard Ziolkowski of the University of Arizona for helpful discretions related to the content of this paper. The authors are deeply indebted to the Canadian Centre for Marine Communications (CCMC) for the extended use of their acoustic tank and equipment at the Marine Institute, St. John's, Newfoundland. The authors also wish to thank Brian McGraw of CCMC for his technical assistance and Leo Spurrell and Humphrey Dye of Memorial University's Technical Services for the machined spheres.

*Present address: Marine Institute, 155 Ridge Road, St. John's, NF, Canada A1C 5R3.

[1] J. B. Brittingham, J. Appl. Phys. **54**, 1179 (1983).
[2] R. W. Ziolkowski, J. Math. Phys. **26**, 861 (1985).
[3] R. W. Ziolkowski, Phys. Rev. A **39**, 2005 (1989).
[4] I. M. Besieris, A. M. Shaarawi, and R. W. Ziolkowski, J. Math. Phys. **30**, 1254 (1989).
[5] P. L. Overfelt, Phys. Rev. A **44**, 3941 (1991).

[6] R. W. Ziolkowski, Phys. Rev. A **44**, 3960 (1991).
[7] J. Lu and J. F. Greenleaf, IEEE Trans. Ultrason. Ferroelect. Freq. Contr. **39**, 441 (1992).
[8] R. Donnelly and R. W. Ziolkowski, Proc. R. Soc. London Ser. A **437**, 673 (1992).
[9] R. Donnelly and R. W. Ziolkowski, Proc. R. Soc. London Ser. A **440**, 541 (1993).
[10] R. W. Ziolkowski, D. K. Lewis, and B. D. Cook, Phys. Rev. Lett. **62**, 147 (1988).
[11] R. W. Ziolkowski and D. K. Lewis, J. Appl. Phys. **68**, 6083 (1990).
[12] R. Donnelly and D. Power, IEEE Antennas Propagation Soc. Int. Symp. Dig. **1**, 82 (1992).
[13] R. Donnelly, D. Power, G. Templeman, and A. Whalen, IEEE Trans. Ultrason. Ferroelect. Freq. Contr. (to be published).
[14] P. Morse and K. U. Ingard, *Theoretical Acoustics* (McGraw-Hill, New York, 1968), pp. 422–425.
[15] *American Institute of Physics Handbook,* 3rd ed., edited by D. E. Gray (McGraw-Hill, New York, 1972), pp. (3-100)–(3-107).
[16] D. S. Jones, *The Theory of Electromagnetism* (Pergamon, New York, 1964), pp. 38–42.